A generalized plasticity model for the stress-strain and creep behavior of rockfill materials

FU ZhongZhi[1*], CHEN ShengShui[2] & WEI KuangMin[1]

[1] *Geotechnical Engineering Department, Nanjing Hydraulic Research Institute, Nanjing 210024, China;*
[2] *Key Laboratory of Failure Mechanism and Safety Control Techniques of Earth-rock Dam, Nanjing 210029, China*

The generalized plasticity constitutive equations that simulate, in a unified manner, the stress-strain response and the creep behavior of rockfill materials are derived using the concept of elastoplasticity. A single yield surface is assumed to capture the onset of plastic strains with, however, two separate potential functions for the stress-induced plastic strains and the creep strains, respectively. The involved tensors and scalars are then specified directly, following the generalized plasticity method, to substantiate the constitutive equations. The model thus obtained is verified using triaxial compression experiments, true triaxial experiments and triaxial creep experiments. The effectiveness of the model is also demonstrated by a successful application in studying the behavior of a high concrete face rockfill dam (CFRD). It is found that for a high CFRD with a long construction period, neglecting the creep of rockfill materials during construction results in an underestimation of the deformation of the dam. The deformation and stress of the concrete slabs may also be considerably underestimated.

rockfill materials, creep behavior, constitutive model, generalized plasticity, concrete face rockfill dam (CFRD)

1   Introduction

A concrete face rockfill dam (CFRD) is a type of infrastructure widely used in water resource management and hydropower exploitation all around the world. The concrete slabs, supported and stabilized by the underlying rockfill materials, are connected with the toe plinth by perimetric joints to form the impermeable system [1]. Due to the adaptability to different topographical and geological conditions and the economical advantage of utilizing local materials, the CFRD has become a competitive alternative to concrete dams [2]. The height of modern CFRDs has grown from 100 m to 200 m in the past few decades. In addition, many weak rocks, which were conventionally considered inappropriate for CFRDs, have also been successfully used in modern CFRDs [3,4].

The increase in the dam height and the extensive use of weak rocks turn the long-term deformation (creep) of CFRDs into an important issue that deserves full consideration in the designing process [5]. Many efforts have been made to establish, on the basis of available field settlement observations, an empirical formula expressing the crest settlement as a function of the dam height and other factors [6–8]. The uniqueness of the dam materials, the engineering geology, the topographical conditions and the working environments in each particular project, however, often invalidate such empirical equations [6]. The crest settlement in itself cannot provide any indication about the performance and safety of the impermeable systems.

With the development of numerical techniques, especially the successful application of the finite element method in engineering, a great amount of effort has also been devoted

*Corresponding author (email: fu_zhongzhi@yahoo.com)

to modeling the elementary creep behavior of rockfill materials using different approaches [9–14]. These models can be roughly classified into two categories. The first one can be termed empirical models [9–11], in which empirical formulas expressing the final amounts of creep strains or their rates as functions of stress states and time are established based on experimental observations. These models are generally used as complements to static constitutive models of rockfill materials, and the loading-induced deformation and long-term creep of the concerned dams are investigated separately.

Advanced models have also been proposed within different frameworks such as elastoplasticity [12,15,16] and hypoplasticity [13,14]. Models in this category are generally extensions of existing ones, and the mechanism underlying the creep behavior is rationally, at least partially, reflected. For instance, the degradation of the solid hardness is thought to be the reason that triggers the creep of rockfill materials [13]. Moreover, these models are capable of modeling the stress-induced strains and the creep strains in a unified manner, which is necessary in high CFRDs with a long construction duration [17]. The involved parameters, however, are generally more difficult to calibrate than those in empirical models, which to some extent sacrifices their applicability in engineering practice.

In this study, a practical constitutive model considering the creep behavior of rockfill materials is proposed in the framework of generalized plasticity [18]. By defining the loading direction tensor, the plastic flow direction tensor and the plastic modulus directly without recourses to any particular yield and plastic potential functions and hardening laws, the generalized plasticity gains a large amount of flexibility in modeling the complex behavior of soils [19–21]. The work described herein can be seen as another application of this theoretical framework. The general form of constitutive equations taking into account the creep behavior of rockfill materials is derived using the concepts of elastoplasticity. The constitutive equations are then substantiated in the light of experimental and field observations. Verification of the proposed model is conducted using some published experimental data, and the model is used in studying the behavior of a high CFRD. Throughout this paper, compressive stresses and strains are defined as positive, and all the normal stresses are effective ones although the conventional comma in soil mechanics is omitted.

2   Generalized plasticity constitutive equations

Although a yield function, a plastic potential function and a hardening law are not required in a generalized plasticity model, the final constitutive equation is of the same structure as that in classical elastoplastic models, and the concept in

the latter could be employed in deriving the constitutive equation for the former. For example, the total strain increment, $d\boldsymbol{\varepsilon}$, in a generalized plasticity model could also be decomposed into an elastic part and a plastic part:

$$d\boldsymbol{\varepsilon} = d\boldsymbol{\varepsilon}^{e} + d\boldsymbol{\varepsilon}^{p}, \tag{1}$$

in which the superscripts e and p denote elastic and plastic, respectively.

Since creep strains occur in rockfill materials even when the stress is kept constant, a new state variable, other than stresses, should be included in the yield function so that the sole variation of this state variable can also result in an expansion of the yield surface and thus plastic strains. Figure 1 is a schematic illustration of such an extended yield surface, upon which a change of the state variable s along the path AB needs an expansion of the current yield surface. As a result, plastic strains are bound to occur. Based on this concept, the yield function may be of the following form:

$$F(\boldsymbol{\sigma}, s, h) = 0, \tag{2}$$

in which $\boldsymbol{\sigma}$ is the stress tensor, s is the additional state variable that changes with time and h denotes the hardening parameter that controls the size of the yield surface.

As mentioned above, plastic strains can be caused not only by a change in the stress state but also by a change in the state variable. However, given the same stress state, the direction of stress-induced plastic strains may differ from that of creep strains. It was found by different authors that the creep strains of rockfill materials and sands could be considerably more contractive compared with the loading-induced strains at the same stress state [22–24]. This fact indicates that two different flow rules should be employed for the stress-induced plastic strains and the creep strains. To this end, two plastic potential functions can be used separately as follows:

$$G_{L}(\boldsymbol{\sigma}, s, h) = 0; \quad G_{C}(\boldsymbol{\sigma}, s, h) = 0, \tag{3}$$

in which G_{L} governs the loading-induced plastic flow and G_{C} governs the plastic strains caused by the change of the state variable s, i.e., creep in this study. It is a unique concept in which a single yield function is used to judge the onset of plastic strains with two separate plastic potential functions for plastic strains of different origins.

The plastic potential functions given in eq. (3) determine the incremental plastic strains as follows:
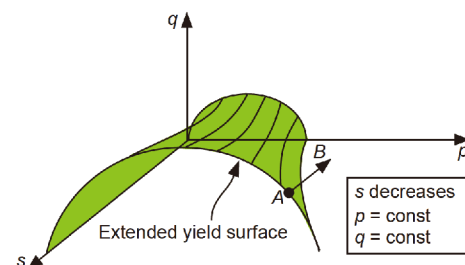

Figure 1   (Color online) Illustration of the extended yield surface.

$$d\boldsymbol{\varepsilon}^{p} = \lambda_{L}\frac{\partial G_{L}}{\partial \boldsymbol{\sigma}} + \lambda_{C}\frac{\partial G_{C}}{\partial \boldsymbol{\sigma}}, \tag{4}$$

in which λ_{L} and λ_{C} are two scalars that control the magnitudes of plastic strains.

The so called consistency condition can be derived from eq. (1), i.e.,

$$\frac{\partial F}{\partial \boldsymbol{\sigma}} : d\boldsymbol{\sigma} + \frac{\partial F}{\partial s}ds + \frac{\partial F}{\partial h}dh = 0, \tag{5}$$

in which the colon (:) denotes the double dot product of two tensors. The incremental stress $d\boldsymbol{\sigma}$ can be evaluated using the elastic tensor and the elastic strain increments:

$$d\boldsymbol{\sigma} = \mathbf{D}^{e} : d\boldsymbol{\varepsilon}^{e} = \mathbf{D}^{e} : (d\boldsymbol{\varepsilon} - d\boldsymbol{\varepsilon}^{p}), \tag{6}$$

where $\mathbf{D}^{e}$ denotes the fourth-order elastic tensor.

The hardening parameter introduced in the yield function and the plastic potential functions generally depends on the plastic strains and the state variable; therefore, dh in eq. (5) can be expressed as follows:

$$dh = \frac{\partial h}{\partial \boldsymbol{\varepsilon}^{p}} : d\boldsymbol{\varepsilon}^{p} + \frac{\partial h}{\partial s}ds. \tag{7}$$

Inserting eq. (4) into eq. (6) and multiplying by $\partial F/\partial \boldsymbol{\sigma}$ on both sides of eq. (6) yields

$$\frac{\partial F}{\partial \boldsymbol{\sigma}} : d\boldsymbol{\sigma} = \frac{\partial F}{\partial \boldsymbol{\sigma}} : \mathbf{D}^{e} : d\boldsymbol{\varepsilon} - \lambda_{L}\frac{\partial F}{\partial \boldsymbol{\sigma}} : \mathbf{D}^{e} : \frac{\partial G_{L}}{\partial \boldsymbol{\sigma}}$$
$$- \lambda_{C}\frac{\partial F}{\partial \boldsymbol{\sigma}} : \mathbf{D}^{e} : \frac{\partial G_{C}}{\partial \boldsymbol{\sigma}}, \tag{8}$$

which can be substituted, together with eq. (7), into eq. (5) to yield the following consistency equation:

$$\frac{\partial F}{\partial \boldsymbol{\sigma}} : \mathbf{D}^{e} : d\boldsymbol{\varepsilon} - \lambda_{L}\frac{\partial F}{\partial \boldsymbol{\sigma}} : \mathbf{D}^{e} : \frac{\partial G_{L}}{\partial \boldsymbol{\sigma}} - \lambda_{C}\frac{\partial F}{\partial \boldsymbol{\sigma}} : \mathbf{D}^{e} : \frac{\partial G_{C}}{\partial \boldsymbol{\sigma}}$$
$$+ \frac{\partial F}{\partial s}ds + \frac{\partial F}{\partial h}\frac{\partial h}{\partial \boldsymbol{\varepsilon}^{p}} : d\boldsymbol{\varepsilon}^{p} + \frac{\partial F}{\partial h}\frac{\partial h}{\partial s}ds = 0. \tag{9}$$

It is clear that a single consistency condition cannot yield the expressions of the two scalar variables λ_{L} and λ_{C}. However, a sufficient condition that always satisfies eq. (9) can be used instead, that is

$$\begin{cases} \lambda_{L}\frac{\partial F}{\partial h}\frac{\partial h}{\partial \boldsymbol{\varepsilon}^{p}} : \frac{\partial G_{L}}{\partial \boldsymbol{\sigma}} - \lambda_{L}\frac{\partial F}{\partial \boldsymbol{\sigma}} : \mathbf{D}^{e} : \frac{\partial G_{L}}{\partial \boldsymbol{\sigma}} \\ \quad + \frac{\partial F}{\partial \boldsymbol{\sigma}} : \mathbf{D}^{e} : d\boldsymbol{\varepsilon} - \lambda_{C}\frac{\partial F}{\partial \boldsymbol{\sigma}} : \mathbf{D}^{e} : \frac{\partial G_{C}}{\partial \boldsymbol{\sigma}} = 0, \\ \lambda_{C}\frac{\partial F}{\partial h}\frac{\partial h}{\partial \boldsymbol{\varepsilon}^{p}} : \frac{\partial G_{C}}{\partial \boldsymbol{\sigma}} + \frac{\partial F}{\partial s}ds + \frac{\partial F}{\partial h}\frac{\partial h}{\partial s}ds = 0, \end{cases} \tag{10}$$

from which the representations of the two scalar factors in eq. (4) can be obtained, i.e.,

$$\begin{cases} \lambda_{L} = \dfrac{\dfrac{\partial F}{\partial \boldsymbol{\sigma}} : \mathbf{D}^{e} : d\boldsymbol{\varepsilon} - \lambda_{C}\dfrac{\partial F}{\partial \boldsymbol{\sigma}} : \mathbf{D}^{e} : \dfrac{\partial G_{C}}{\partial \boldsymbol{\sigma}}}{\dfrac{\partial F}{\partial \boldsymbol{\sigma}} : \mathbf{D}^{e} : \dfrac{\partial G_{L}}{\partial \boldsymbol{\sigma}} - \dfrac{\partial F}{\partial h}\dfrac{\partial h}{\partial \boldsymbol{\varepsilon}^{p}} : \dfrac{\partial G_{L}}{\partial \boldsymbol{\sigma}}}, \\[2em] \lambda_{C} = -\dfrac{\dfrac{\partial F}{\partial s} + \dfrac{\partial F}{\partial h}\dfrac{\partial h}{\partial s}}{\dfrac{\partial F}{\partial h}\dfrac{\partial h}{\partial \boldsymbol{\varepsilon}^{p}} : \dfrac{\partial G_{C}}{\partial \boldsymbol{\sigma}}}ds. \end{cases} \tag{11}$$

By replacing the two scalars in eq. (4) with those given in

eq. (11) and substituting the result into eq. (6), the final constitutive equation can be obtained as follows:

$$d\boldsymbol{\sigma} = \left[\mathbf{D}^{e} - \frac{\left(\mathbf{D}^{e} : \dfrac{\partial G_{L}}{\partial \boldsymbol{\sigma}}\right) \otimes \left(\dfrac{\partial F}{\partial \boldsymbol{\sigma}} : \mathbf{D}^{e}\right)}{\dfrac{\partial F}{\partial \boldsymbol{\sigma}} : \mathbf{D}^{e} : \dfrac{\partial G_{L}}{\partial \boldsymbol{\sigma}} - \dfrac{\partial F}{\partial h}\dfrac{\partial h}{\partial \boldsymbol{\varepsilon}^{p}} : \dfrac{\partial G_{L}}{\partial \boldsymbol{\sigma}}}\right]$$
$$: \left(d\boldsymbol{\varepsilon} + \frac{\dfrac{\partial F}{\partial s} + \dfrac{\partial F}{\partial h}\dfrac{\partial h}{\partial s}}{\dfrac{\partial F}{\partial h}\dfrac{\partial h}{\partial \boldsymbol{\varepsilon}^{p}} : \dfrac{\partial G_{C}}{\partial \boldsymbol{\sigma}}} : \dfrac{\partial G_{C}}{\partial \boldsymbol{\sigma}}ds\right). \tag{12}$$

By introducing the following notations:

$$\mathbf{n}_{L} = \frac{\dfrac{\partial G_{L}}{\partial \boldsymbol{\sigma}}}{\left\|\dfrac{\partial G_{L}}{\partial \boldsymbol{\sigma}}\right\|}; \quad \mathbf{n}_{C} = \frac{\dfrac{\partial G_{C}}{\partial \boldsymbol{\sigma}}}{\left\|\dfrac{\partial G_{C}}{\partial \boldsymbol{\sigma}}\right\|}; \quad \mathbf{n}_{F} = \frac{\dfrac{\partial F}{\partial \boldsymbol{\sigma}}}{\left\|\dfrac{\partial F}{\partial \boldsymbol{\sigma}}\right\|};$$
$$H_{L} = -\frac{\dfrac{\partial F}{\partial h}\dfrac{\partial h}{\partial \boldsymbol{\varepsilon}^{p}} : \mathbf{n}_{L}}{\left\|\dfrac{\partial F}{\partial \boldsymbol{\sigma}}\right\|}; \quad H_{C} = -\frac{\dfrac{\partial F}{\partial h}\dfrac{\partial h}{\partial \boldsymbol{\varepsilon}^{p}} : \mathbf{n}_{C}}{\dfrac{\partial F}{\partial s} + \dfrac{\partial F}{\partial h}\dfrac{\partial h}{\partial s}}. \tag{13}$$

Eq. (12) can be rewritten in a simplified form:

$$d\boldsymbol{\sigma} = \left[\mathbf{D}^{e} - \frac{\left(\mathbf{D}^{e} : \mathbf{n}_{L}\right) \otimes \left(\mathbf{n}_{F} : \mathbf{D}^{e}\right)}{\mathbf{n}_{F} : \mathbf{D}^{e} : \mathbf{n}_{L} + H_{L}}\right] : \left(d\boldsymbol{\varepsilon} - \frac{1}{H_{C}}\mathbf{n}_{C}ds\right). \tag{14}$$

Note that the Euclidean norm of a tensor in eq. (13) is defined as $\|\boldsymbol{n}\| = (n_{ij}n_{ij})^{1/2}$, in which the summation over repeated indices (i & j) is taken.

The constitutive equation can also be expressed in an inverse form. To this end, eq. (10) is rewritten as follows:

$$\begin{cases} \lambda_{L}\dfrac{\partial F}{\partial h}\dfrac{\partial h}{\partial \boldsymbol{\varepsilon}^{p}} : \dfrac{\partial G_{L}}{\partial \boldsymbol{\sigma}} + \dfrac{\partial F}{\partial \boldsymbol{\sigma}} : d\boldsymbol{\sigma} = 0, \\ \lambda_{C}\dfrac{\partial F}{\partial h}\dfrac{\partial h}{\partial \boldsymbol{\varepsilon}^{p}} : \dfrac{\partial G_{C}}{\partial \boldsymbol{\sigma}} + \left(\dfrac{\partial F}{\partial s} + \dfrac{\partial F}{\partial h}\dfrac{\partial h}{\partial s}\right)ds = 0, \end{cases} \tag{15}$$

from which the two scalars can be obtained, i.e.,

$$\lambda_{L} = \frac{\mathbf{n}_{F} : d\boldsymbol{\sigma}}{H_{L}\|\partial G_{L}/\partial \boldsymbol{\sigma}\|}; \quad \lambda_{C} = \frac{ds}{H_{C}\|\partial G_{C}/\partial \boldsymbol{\sigma}\|}. \tag{16}$$

Substituting eq. (16) into eq. (4) and inserting the resultant eq. (4) into the inverse form of eq. (6) yields the following stress-driven constitutive equation:

$$d\boldsymbol{\varepsilon} = \left[(\mathbf{D}^{e})^{-1} + \frac{\mathbf{n}_{L} \otimes \mathbf{n}_{F}}{H_{L}}\right] : d\boldsymbol{\sigma} + \frac{1}{H_{C}}\mathbf{n}_{C}ds. \tag{17}$$

It can be seen that if the boundary of a rockfill specimen is restricted so that no strains can develop, i.e., $d\boldsymbol{\varepsilon} = \mathbf{0}$, stress relaxation will occur due to the change of the state variable. On the other hand, if the stress state is kept constant, i.e., $d\boldsymbol{\sigma} = \mathbf{0}$, the material will undergo additional strains when the state variable changes. Therefore, eqs. (14) and (17) can describe the stress relaxation and creep behavior of rockfill materials in a unified manner. In addition, the strains caused by stress and creep can also be modeled simultaneously.

3　Substantiation of the constitutive equations

As seen from eqs. (14) and (17), modeling the loading and creep behaviors of rockfill materials within the framework of generalized plasticity can be fulfilled by defining three direction tensors and two moduli scalars as well as an elastic tensor. Conventional mechanical tests (without creep), such as triaxial compression experiments, can be used to determine $\mathbf{D}^e$, $\boldsymbol{n}_L$, $\boldsymbol{n}_F$, and H_L, and creep experiments (under constant stress states) can be used to determine the creep strain direction tensor $\mathbf{n}_C$ and the creep modulus H_C. In this section, these scalars and tensors are specified to fulfill the constitutive equations.

3.1　Substantiation of the basic constitutive equation

In the following section, the former four variables are defined to substantiate the basic constitutive model that neglects the creep-related terms. The strain invariants below:

$$\begin{cases} d\varepsilon_v^p = d\varepsilon_{ij}^p \delta_{ij}, \\ d\varepsilon_s^p = \sqrt{\dfrac{2}{3}\left(d\varepsilon_{ij}^p - \dfrac{1}{3}d\varepsilon_v^p\delta_{ij}\right)\left(d\varepsilon_{ij}^p - \dfrac{1}{3}d\varepsilon_v^p\delta_{ij}\right)}, \end{cases} \quad (18)$$

and stress notations

$$p = \frac{\mathrm{tr}(\boldsymbol{\sigma})}{3}; \quad \mathbf{s} = \boldsymbol{\sigma} - p\mathbf{I}; \quad q = \sqrt{2\mathbf{s}:\mathbf{s}/3}; \quad \eta = \frac{q}{p} \quad (19)$$

are used hereafter. Herein, $d\varepsilon_v^p$ and $d\varepsilon_s^p$ denote the increments of plastic volumetric and deviatoric strains, respectively. p, q and η denote the mean effective stress, the generalized shear stress and the stress ratio; $\mathbf{s}$ and $\mathbf{I}$ denote the stress deviator and the second-order unit tensor, respectively. The operation $\mathrm{tr}(\cdot)$ means the trace of a second-order tensor.

3.1.1　Stress-induced plastic flow direction tensor
The normalized plastic flow direction tensor can be expressed as follows:

$$\mathbf{n}_L = \frac{d\boldsymbol{\varepsilon}^p}{\|d\boldsymbol{\varepsilon}^p\|}, \quad (20)$$

in which the Euclidean norm of the plastic strain tensor is defined as $\|d\boldsymbol{\varepsilon}^p\| = (d\varepsilon_{ij}^p d\varepsilon_{ij}^p)^{1/2}$. The incremental plastic strain tensor can be expressed using the volumetric strain ($d\varepsilon_v^p$) and the deviatoric strain ($d\varepsilon_s^p$), i.e.,

$$d\boldsymbol{\varepsilon}^p = d\varepsilon_v^p\frac{\mathbf{I}}{3} + d\varepsilon_s^p\frac{3\mathbf{s}}{2q} = d\varepsilon_s^p\left(\frac{d}{3}\mathbf{I} + \frac{3}{2q}\mathbf{s}\right), \quad (21)$$

where $d = d\varepsilon_v^p/d\varepsilon_s^p$ is the dilatancy ratio.

Inserting eq. (21) into eq. (20) yields

$$\mathbf{n}_L = \pm\left(d\frac{\mathbf{I}}{3} + \frac{3\mathbf{s}}{2q}\right)\Big/\sqrt{\frac{1}{3}d^2 + \frac{3}{2}}, \quad (22)$$

in which the sign of the right-hand side depends on the sign of the deviatoric strain. If $d\varepsilon_s^p > 0$, then the positive one will

be used; otherwise, the negative branch should be used instead. It is worth noting that these volumetric and deviatoric strains are stress induced strains that do not include the contribution of creep.

The dilatancy ratio is a function of the stress state. Herein, the following linear equation is used to model the shear dilation behavior of rockfill materials in triaxial compression stress states [21]:

$$d = d_0\left(1 - \frac{\eta}{M_d}\right), \quad (23)$$

where d_0 is a parameter and M_d is the constant volume stress ratio, exceeding which the material starts to dilate. The representation of M_d under a triaxial compression stress state reads:

$$M_d = \frac{6\sin\psi}{3 - \sin\psi}, \quad (24)$$

in which the constant volume friction angle, ψ, depends on the confining stress, σ_3, as follows [21]:

$$\psi = \psi_0 - \Delta\psi\lg\frac{\sigma_3}{p_a}, \quad (25)$$

where ψ_0 and $\Delta\psi$ are two parameters and p_a denotes the atmospheric pressure.

Recently, Xiao et al. [25,26] studied the particle breakage and resultant dilatancy behavior of rockfill materials under general stress states using a true triaxial apparatus. Similar to experimental findings made on sands, the clear influence of the intermediate principal stress was also observed. The stress dilatancy relationship of granular materials under triaxial extension differs from that under triaxial compression in two aspects [27–29]. First, the stress ratio at which the volumetric strain vanishes is lower in triaxial extension tests than in triaxial compression tests, as shown in Figure 2, which is reproduced using the data by Nakai [27]. Second, the regression line in triaxial extension states is less steep than that in triaxial compression states. Similar trends have also been noticed by other authors [28,29]. It is reasonable to parallel these observations in establishing the stress dilatancy equation for rockfill materials under complex stress states. To this end, eq. (24) is extended to the following generalized form:
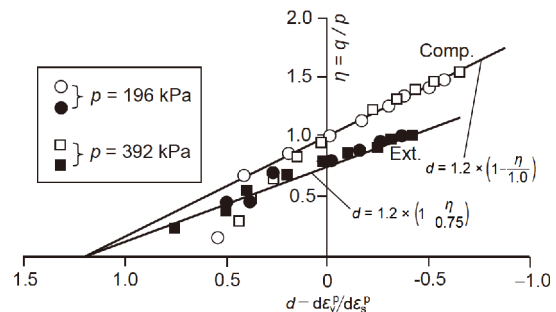

Figure 2　Stress dilatancy data in triaxial compression and extension tests.

$$d = d_0 \left[1 - \frac{q}{g(\theta) \cdot M_d \cdot p} \right], \tag{26}$$

in which the function $g(\theta)$ is used to reflect the dependence of the dilatancy ratio upon stress states, and the definition of the Lode angle, θ, is given as follows [13,14]:

$$\cos 3\theta = -\sqrt{6} \frac{\text{tr}(\mathbf{s} \cdot \mathbf{s} \cdot \mathbf{s})}{\|\mathbf{s}\|^3}. \tag{27}$$

Eq. (27) produces a value of $\theta = 0$ under triaxial extension states and $\theta = \pi/3$ under triaxial compression states. Therefore, the condition $g(\pi/3) = 1$ should be fulfilled in establishing the function $g(\theta)$. The representation of $g(\theta)$ is derived in the Appendix, and the result is given below:

$$g(\theta) = \frac{q}{2p} \left(\frac{1}{\sin\varphi_m} - \frac{1}{3} \right), \tag{28}$$

in which φ_m is the mobilized friction angle. The function $g(\theta)$ is also used in modeling the dependence of the shear strength on the stress states.

3.1.2   Loading direction tensor

In the classical elastoplasticity theory, the loading direction is defined using a yield function, and the flow rule is associative if the plastic potential function is the same as the yield function or if the plastic direction tensor is identical to the loading direction tensor. Many experiments have shown that a non-associative flow rule might be more suitable for granular materials such as sands and rockfills than an associative flow rule [30]. However, in this study, the plastic flow direction tensor is used as the loading direction tensor to ensure a symmetric elastoplastic tensor and thus a symmetric stiffness tensor. Considerable memory and computational capacity can be saved when an associative flow rule is used in solving boundary value problems using a finite element procedure. Another consequence of such a simplification is the possibility of neglecting the negative branch of eq. (22) in forming the fourth-order elastoplastic tensor according to eq. (14).

3.1.3   Elastic modulus and elastic tensor

The simplest isotropic elastic model is used herein to describe the elastic behavior of rockfill materials [31], i.e.,

$$D_{ijkl}^e = \frac{v_e \cdot E_e}{(1+v_e)(1-2v_e)} \delta_{ij}\delta_{kl} + \frac{E_e}{2(1+v_e)} \left(\delta_{ik}\delta_{jl} + \delta_{il}\delta_{jk} \right), \tag{29}$$

in which E_e and v_e denote the Young's modulus and the Poisson's ratio, respectively. δ_{ij} is the Kronecker sign.

Unloading experiments conducted in triaxial apparatuses show that the elastic modulus of a rockfill depends on the confining stress, while it is almost not influenced by the deviatoric stress level from which the specimen is unloaded. Therefore, the following power function is adopted for the elastic modulus [32]:

$$E_e = k_{au} \cdot p_a \cdot \left(\frac{\sigma_3}{p_a} \right)^n, \tag{30}$$

in which k_{au} and n are two parameters. The Poisson's ratio of coarse rockfill materials is relatively difficult to calibrate. For practical problems, however, it can be assumed to be a constant for simplicity, e.g., $v_e \approx 0.3$.

3.1.4   Plastic modulus scalar

Triaxial experiments also show that the tangential loading modulus, E_t, depends not only on the confining stress but also on the shear stress level, and the following equation is used herein [21]:

$$E_t = \left(1 - \frac{\eta}{M_f} \right)^\alpha \cdot k \cdot p_a \cdot \left(\frac{\sigma_3}{p_a} \right)^n, \tag{31}$$

where k and α are two other parameters. M_f is the peak stress ratio at which the tested material fails. Under a triaxial compression stress state, the peak stress ratio reads:

$$M_f = \frac{6\sin\varphi}{3 - \sin\varphi}, \tag{32}$$

in which the peak friction angle, φ, also depends on the confining stress, σ_3, as follows [21]:

$$\varphi = \varphi_0 - \Delta\varphi \lg\frac{\sigma_3}{p_a}, \tag{33}$$

where φ_0 and $\Delta\varphi$ are two other friction parameters.

The strength of rockfill materials under triaxial extension stress states also differs from that under triaxial compression states; i.e., the values of the peak stress ratio under both conditions are not the same [33–35]. However, the tangential modulus given in eq. (31) implicates a cone-shaped failure surface in the principal stress space and a unique peak stress ratio independent of the stress states, which may considerably overestimate the peak strength of materials under complex stress states [34]. To eliminate this deficiency, eq. (31) is also extended to the following general form:

$$E_t = \left[1 - \frac{q}{g(\theta) \cdot M_f \cdot p} \right]^\alpha \cdot k \cdot p_a \cdot \left(\frac{\sigma_3}{p_a} \right)^n, \tag{34}$$

in which the function $g(\theta)$ given in eq. (28) is similarly embedded.

To establish the representation of the plastic modulus, the special form of the constitutive equation under a triaxial compression stress state ($\sigma_1 > \sigma_2 = \sigma_3$) is used, i.e.,

$$
\begin{pmatrix} d\varepsilon_1 \\ d\varepsilon_2 \\ d\varepsilon_3 \end{pmatrix} = \frac{1}{E_e} \begin{bmatrix} 1 & -v_e & -v_e \\ -v_e & 1 & -v_e \\ -v_e & -v_e & 1 \end{bmatrix} \begin{pmatrix} d\sigma_1 \\ d\sigma_2 \\ d\sigma_3 \end{pmatrix}
$$
$$
+ \frac{1}{H_L(3/2 + d^2/3)} \begin{pmatrix} d/3 + 1 \\ d/3 - 1/2 \\ d/3 - 1/2 \end{pmatrix}
$$
$$
\times \begin{pmatrix} d/3 + 1 \\ d/3 - 1/2 \\ d/3 - 1/2 \end{pmatrix}^{\text{T}} \begin{pmatrix} d\sigma_1 \\ d\sigma_2 \\ d\sigma_3 \end{pmatrix}. \tag{35}
$$

Under the loading condition $d\sigma_1 > d\sigma_2 = d\sigma_3 = 0$, the first line

of eq. (35) can be expressed as follows:

$$\frac{1}{E_t} = \frac{d\varepsilon_1}{d\sigma_1} = \frac{1}{E_e} + \frac{(1+d/3)^2}{H_L(3/2+d^2/3)}, \tag{36}$$

from which the following representation of plastic modulus can be obtained:

$$H_L = \frac{(1+d/3)^2}{(3/2+d^2/3)}\left(\frac{1}{E_t} - \frac{1}{E_e}\right)^{-1}. \tag{37}$$

It can be verified that when $q/[g(\theta)\cdot M_f\cdot p]$ approaches 1, the tangential modulus and the plastic modulus vanish, and infinite plastic strains will occur.

There are 10 parameters in the basic model, i.e., the peak friction angle parameters (φ_0 and $\Delta\varphi$), the dilatancy parameters (d_0, ψ_0 and $\Delta\psi$), the tangential modulus parameters (k, n and α), and the elasticity parameters (k_{au} and v_e). These four groups of parameters can be determined by conducting a series of triaxial compression experiments incorporating unloading processes. The basic model as well as the parameters can be used solely in predicting the deformation behavior of CFRDs and other earth and rockfill structures.

3.2   Substantiation of the creep equation

Eqs. (14) and (17) indicate that modeling the creep behavior of rockfill materials needs the specification of a creep flow direction tensor $\mathbf{n}_C$ and a creep modulus scalar H_C. Herein, both variables are defined to complete this task.

3.2.1   *Creep induced plastic flow direction tensor*
Theoretically, the creep flow direction tensor may have the same structure as eq. (22). However, creep tests show that a loaded rockfill specimen always experiences a volume contraction during creeping [23]. Therefore, eq. (22) is slightly modified herein, i.e.,

$$\mathbf{n}_C = \left(\frac{\mathbf{I}}{3} + \frac{3c}{2q}\mathbf{s}\right)\Big/\sqrt{\frac{1}{3}+\frac{3}{2}c^2}, \tag{38}$$

in which c is a proportionality controlling the ratio between deviatoric creep strain and volumetric creep strain.

Creep experiments also show that the flow direction does not keep constant but evolves continuously during creep [22–24], and this is interpreted as the result of the fabric effect [23]. Modeling such a change in direction of creep strains is difficult at this stage, and therefore, it is assumed that the creep strains develop proportionally under constant stresses. A similar assumption has also been used in modeling the wetting-induced strains of rockfill materials [13,14]. As a result, the coefficient c in eq. (38) is constant under a given stress state, and eq. (17) can be reduced to

$$d\boldsymbol{\varepsilon} = \frac{1}{H_C}\mathbf{n}_C ds, \tag{39}$$

which can be integrated to give the final creep strain tensor:

$$\boldsymbol{\varepsilon}_f = \int_0^\infty d\boldsymbol{\varepsilon} = \mathbf{n}_C\int_0^\infty \frac{1}{H_C}dt, \tag{40}$$

where the subscript f signifies the final amounts of creep strains after the creep experiments, and time t is selected as the state variable for simplicity. eq. (40) indicates that if the final volumetric strain and deviatoric strain can be obtained by experiments, then the coefficient c in eq. (38) can be evaluated as follows:

$$c = \frac{\varepsilon_{s,f}}{\varepsilon_{v,f}}. \tag{41}$$

Li et al. [36] conducted a series of creep experiments on rockfill materials used in a CFRD and studied the relationships between the final creep strains and the stress states. The following empirical formulas were suggested to model the final creep strains:

$$\varepsilon_{v,f} = c_1\left(\frac{\sigma_3}{p_a}\right)^{m_1} + c_2\left(\frac{q}{p_a}\right)^{m_2}, \tag{42}$$

and

$$\varepsilon_{s,f} = c_3\left(\frac{\eta}{M_f-\eta}\right)^{m_3}, \tag{43}$$

in which c_1, c_2, c_3, m_1, m_2, and m_3 are six parameters. Eq. (43) indicates that the final deviatoric strain is the same under different confining stresses given the same value of η/M_f, which is contradictory to the experimental finding [11,23]. In this study, eq. (43) is modified as follows:

$$\varepsilon_{s,f} = c_3\left(\frac{\sigma_3}{p_a}\right)^{m_3}\sqrt{\frac{\eta}{M_f-\eta}}, \tag{44}$$

which reflects the influence of the confining stress upon the magnitude of the deviatoric creep strain. Eqs. (42) and (44) are used to define the direction of the creep-induced plastic strains in this study.

3.2.2   *Creep modulus scalar*
Trace operation on both sides of eq. (39) yields:

$$d\varepsilon_v = \frac{1}{H_C}\frac{1}{L_C}dt, \tag{45}$$

in which $L_C = (1/3+3c^2/2)^{1/2}$ and the state variable s has been replaced by the time variable t. It is clear that the determination of the creep modulus needs the relationship between the creep strains and time. However, eqs. (42) and (44) only produce the final amounts of creep strains without describing their evolution histories. It should also be noted that the process of creep deformation in the laboratory differs considerably from that in the field. For example, creep experiments performed in the laboratory often achieve a stable state within 1–2 weeks [22–24]. However, field observations show that the settlement of CFRDs often lasts several years [6,7]. This difference is due to the difficulty in duplicating the *in situ* environment in the laboratory.

Fortunately, vast amounts of field observations are now available, and they provide useful information for understanding the creeping process of CFRDs. For example, field observations made on two hard rock CFRDs and two weak rock CFRDs affirmed that the creep deformation of CFRDs follows an exponential function [17]. It is, therefore, natural to postulate that the creep strains also follow such a function. For instance, the volumetric strain history can be expressed as follows:

$$\varepsilon_v = \varepsilon_{v,f}\left[1 - \exp\left(-\frac{t}{\omega}\right)\right], \tag{46}$$

in which ω is a parameter governing the creep strain rate. The incremental form of eq. (46) reads:

$$d\varepsilon_v = \frac{\varepsilon_{v,f}}{\omega}\exp\left(-\frac{t}{\omega}\right)dt, \tag{47}$$

which can be inserted into eq. (45) to derive the representation of the creep modulus, i.e.,

$$H_C = \frac{\omega}{\varepsilon_{v,f}}\frac{1}{L_C}\exp\left(\frac{t}{\omega}\right) = \frac{1}{L_C}\frac{\omega}{(\varepsilon_{v,f}-\varepsilon_v)}. \tag{48}$$

It can be seen that the creep modulus increases exponentially as time elapses, so that the strain rate decreases rapidly during creeping. The creep modulus can also be derived using the deviatoric strain. However, a volumetric strain based representation is more general since volume contraction always occur in creeping, whereas a deviatoric strain may not present, for instance, under an isotropic stress state.

The creep model established above has 7 additional parameters, among which 6 parameters (c_1–c_3 and m_1–m_3) control the final amounts of creep strains and an additional parameter (ω) governs the creep strain rate. While it is rational to calibrate the former 6 parameters by conducting triaxial creep experiments, the last one cannot be determined reliably by these experimental results as pointed out previously. However, systematic deformation monitoring gauges have been installed in most modern CFRDs, and the collected deformation data can be used to calibrate this parameter effectively and reliably [17].

4 Verification of the proposed model

In this section, the constitutive model established in the previous part will be verified using triaxial compression experiments [37], true triaxial experiments [38] and creep experiments [39] conducted on four kinds of rockfill materials by different authors.
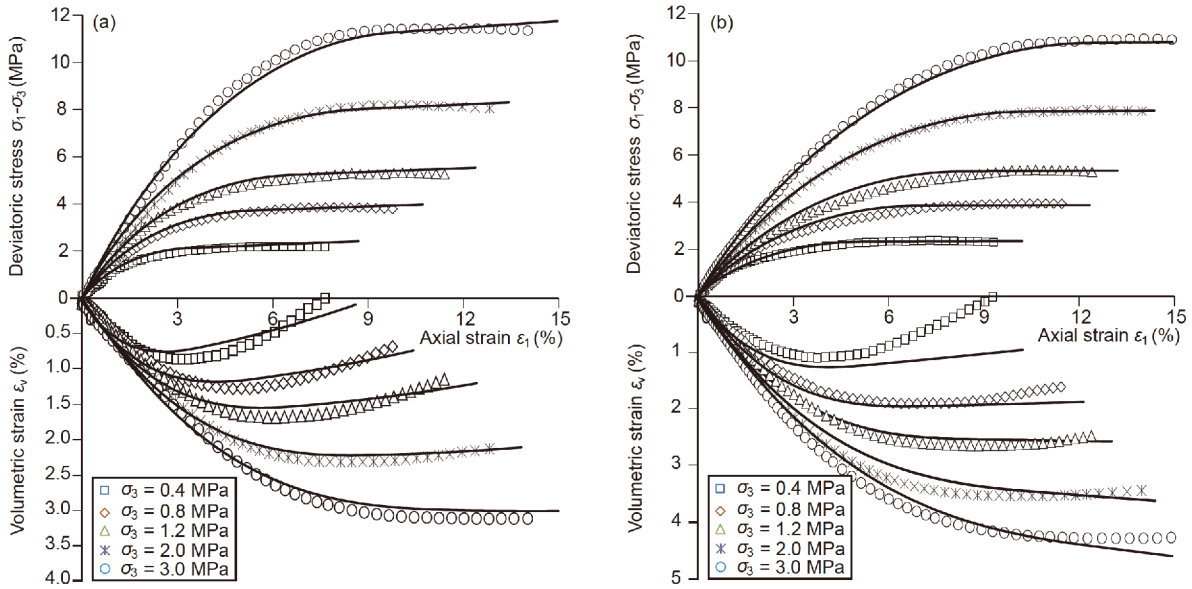
4.1 Modeling triaxial compression experiments

Figure 3 shows the experimental results (dots) obtained from static monotonic triaxial compression experiments on two rockfill materials (termed as rockfill 1 and rockfill 2). Rockfill 1 is a gravelly soil collected from the riverbed of a dam site, and rockfill 2 is excavated explosively from the quarry for the same dam. The basic model parameters calibrated are listed in Table 1. Numerical simulations of these tests are performed, and the obtained results (curves) are also embedded in Figure 3 for comparison. For both materials, all the model predictions agree satisfactorily with the experimental data, including the stress-strain responses and the shear-induced contraction and dilation behavior under different confining pressures.

4.2 Modeling true triaxial experiments

Plotted in Figures 4 and 5 are results of true triaxial experiments conducted by Shi [38] with a rockfill (termed as rockfill 3 herein) used in a high rockfill dam built in China. Two general trends can be observed. First, given the same confining stress, the initial inclination of the (σ_1-σ_3) vs. ε_1 data is steeper in a triaxial extension stress state than in a triaxial compression stress state. In fact, the initial slope of (σ_1-σ_3) vs. ε_1 data increases continuously as the stress state variable b [$=(\sigma_2-\sigma_3)/(\sigma_1-\sigma_3)$] increases from 0 to 1. This finding is in good agreement with the results of true triaxial experiments conducted recently by Rodriguez and Lade [40] with Nevada sands. Second, the peak deviatoric stress also increases continuously when b increases from 0 to 1, which indicates that a higher b value leads to a higher peak friction angle. This finding agrees partially with the results and theory by Lade [33], as the latter suggested an initial increase of the peak friction angle when b is increased from 0 to 0.85, followed by a decrease if b is increased further from 0.85 to 1.
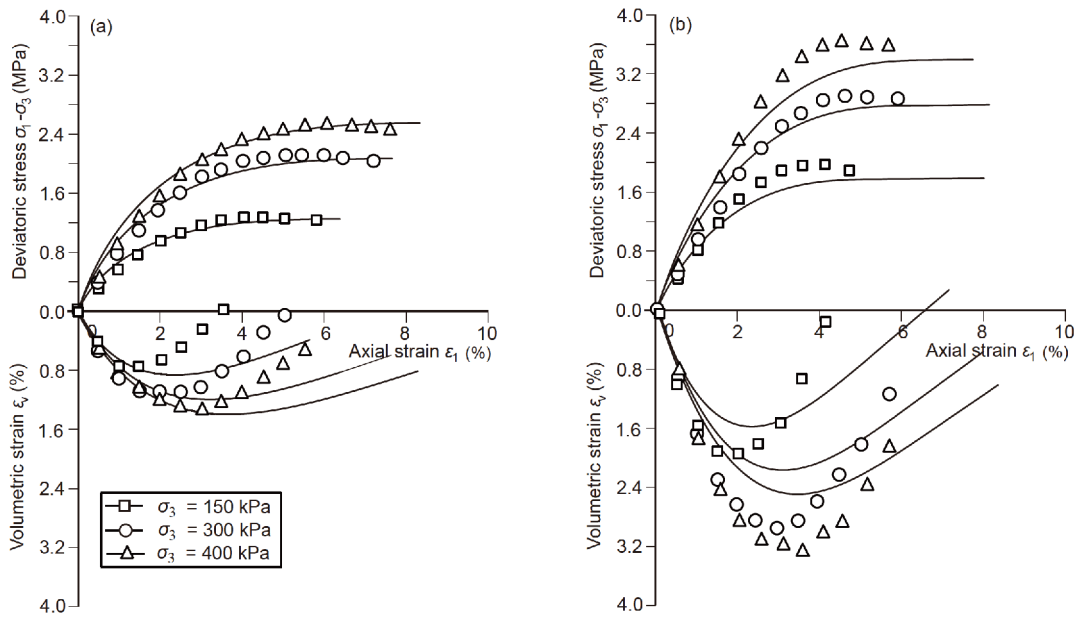
The triaxial compression and extension experiments plotted in Figure 4 are used to calibrate the model parameters, and the obtained results are given in Table 2. Model predictions are also overlapped in the same figure for verification. The predicted (σ_1-σ_3) vs. ε_1 curves agree satisfactorily with the experimental data in both the triaxial compression and extension. However, the agreement of the volumetric strain behavior is relatively poor despite the great effort spent in calibrating the dilatancy parameters. A careful analysis of the original data given by Shi [38] affirms that the second and third principal strains in some triaxial compression experiments (by the true triaxial apparatus) are not identical. The first and second principal strains in some triaxial extension experiments also differ from each other. That is to say, fabric anisotropy might present in some of the specimens. Unsatisfactory volumetric strain data may also be attributed to the relatively low precision of the measured third principal strain. While the first and second principal strains were measured by the displacements of rigid loading plates,

Figure 3   Comparison of model predictions with experimental data from triaxial compression experiments. (a) Rockfill 1; (b) rockfill 2.

Table 1   Basic model parameters of rockfill 1 and rockfill 2

| Material	φ_0 (°)	$\Delta\varphi$ (°)	d_0	ψ_0 (°)	$\Delta\psi$ (°)	k	n	α	k_{au}	v_e
Rockfill 1	50.1	6.3	1.82	46.1	3.5	1214	0.26	0.55	2428	0.3
Rockfill 2	53.2	9.0	2.20	50.5	6.3	879	0.28	0.50	1758	0.3

Figure 4   Model predictions vs. triaxial compression and extension experiments. (a) Triaxial compression; (b) triaxial extension.

the third principal strain was derived from the volume change of the water bags used to apply the minor principal stress. Factors such as the membrane penetration effect and the contacting conditions between water bags and specimens may result in unreliable measurements [38].

Figure 5 shows the comparison of the model predictions with the true triaxial experimental data under 3 different

confining stresses, i.e., $\sigma_3 = 150$ kPa, $\sigma_3 = 300$ kPa and $\sigma_3 = 400$ kPa. The model successfully captures the dependence of the stiffness upon the stress state variable b and the expansion along the direction of the minimum principal stress (σ_3). The evident compressive strain (ε_2) along the direction of intermediate principal stress (σ_2) at a high b value (0.75) and the small magnitude of compressive strain or even tensile
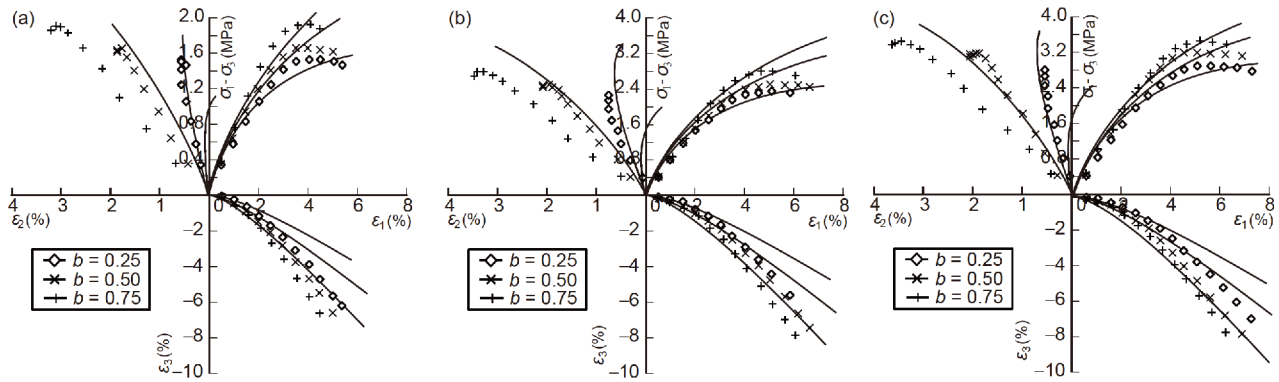
Figure 5 Comparison of model predictions with true triaxial experiments. (a) σ_3=150 kPa; (b) σ_3=300 kPa; (c) σ_3=400 kPa.

Table 2 Basic model parameters of rockfill 3

Material	φ_0 (°)	$\Delta\varphi$ (°)	d_0	ψ_0 (°)	$\Delta\psi$ (°)	k	n	α	k_{au}	v_e
Rockfill 3	55.4	9.6	2.81	51.2	7.3	1100	0.35	0.7	2200	0.20

strain at a low *b* value (0.25) are also successfully reproduced by the model. Although the compressive strain ε_2 is underestimated by the model, different trends at various stress states are successfully captured, which may be seen as an evidence that the performance of the basic model under complex stress states is acceptable.

4.3 Modeling creep experiments

The results of creep experiments conducted by Fu and Ling [39] on a saturated rockfill material (termed as rockfill 4) are plotted in Figures 6 and 7. The dry density of the sample is 2.26 g/cm^3, and the nonlinear friction angles given by the authors are φ_0 = 53.4° and $\Delta\varphi$ = 8.2°. Only some of the experimental data are selected and plotted for the sake of clarity. Creep model parameters calibrated using these results are given in Table 3. Note that c_3 and m_3 are parameters used in eq. (44).

Predictions made by the constitutive model as well as the parameters in Table 3 are also plotted in Figures 6 and 7. In most cases, the model-predicted creep strains, including both the final magnitudes and the accumulation histories, agree satisfactorily with the experimental data. It should be noted that the parameter ω given in Table 2 is determined temporarily by the experimental data to obtain a best fit with the experiments. It does not reflect the real working environment of the tested material in the field, and therefore cannot be used directly for practical problems as mentioned previously.

## 5 Application: Behavior of a high concrete face rockfill dam

The constitutive model established and verified in the previous sections has been incorporated into a finite element

procedure SCAPERS (Stress and Consolidation Analysis Program for Earth and Rockfill Structures), initially developed and continuously updated by the authors [41]. This program has been used in predicting the stress and deformation behavior of a large number of dams in China. In this part, the behavior of the Shuibuya CFRD, which is currently the highest built one of its type, is studied with special attention focused on the deformation and stress behavior of the shell and the concrete slabs. The performance of the Shuibuya CFRD has been studied by several authors, and detailed information can be found in refs. [42–44].

5.1 Finite element model and constitutive parameters

Figure 8 shows the three-dimensional finite element mesh of the dam. The *x*-axis points from the left abutment to the right abutment, and the *y*-axis points from the upstream side to the downstream side. The *z*-axis points upward and is orthogonal to the *x*- and *y*-axes. The dam is discretized with 9694 elements, including 8239 solid elements, 747 interface elements and 508 joint elements. Zero-thickness interface elements are used to model the frictional interaction between the concrete slabs and the cushion layer, and various joint elements are set to model the interaction between the neighboring concrete slabs (known as vertical joints) and that between the concrete slabs and the toe plinth (known as perimetric joints). In numerical simulations, nodes on the left and right truncating boundaries are restricted from axial displacement (along the *x* direction), and the bottom nodes are restricted for all three directions. Hydrostatic pressure is applied on the surface of the concrete slabs.

The construction and impounding processes of the dam is shown in Figure 9, in which the corresponding loading steps in numerical simulations are labeled in parentheses. Due to the unprecedented height of the dam, the concrete slabs are
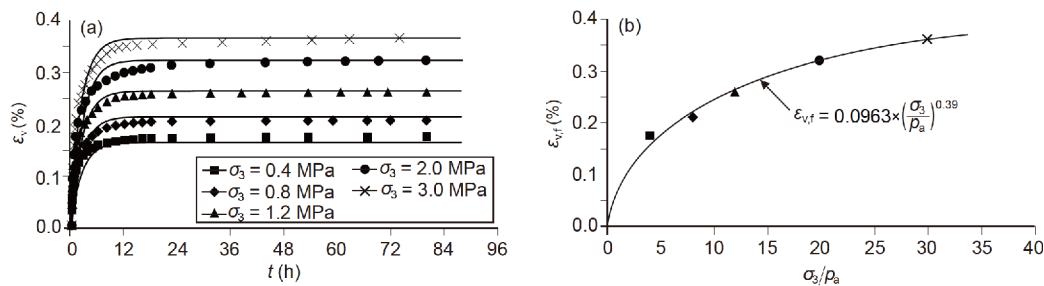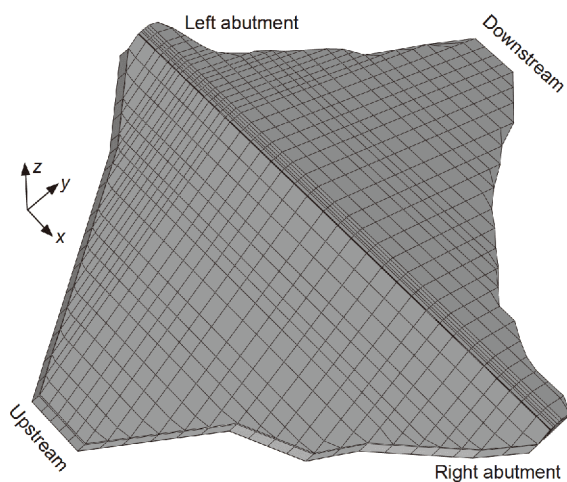
Figure 6   Model predictions vs. creep experiments under isotropic compression stress states. (a) ε_v vs. t; (b) $\varepsilon_{v,f}$ vs. σ_3/p_a.
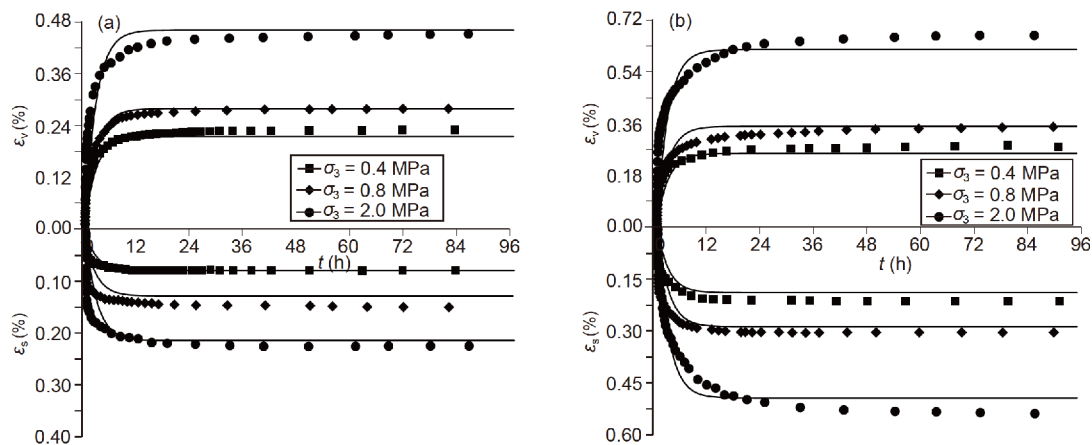
Figure 7   Model predictions vs. creep experiments under shear stress states. (a) $\eta/M_f = 0.4$; (b) $\eta/M_f = 0.8$.

Table 3   Creep model parameters of rockfill 4

| Material	c_1 (%)	m_1	c_2 (%)	m_2	c_3 (%)	m_3	ω (h)
Rockfill 4	0.0963	0.39	0.0047	0.98	0.0416	0.60	2.5

Figure 8   Finite element mesh of the Shuibuya CFRD.

cast to EL. 278.0 m, EL. 340.0 m and EL. 405.0 m in three stages as marked by steps (13) and (14), step (23) and step (34) in Figure 9. During the construction of the dam, several

raises and drawdowns in the reservoir level were experienced as indicated by the arrows in Figure 9. The days taken in each construction step marked in Figure 9 are determined according to the construction records [42].

Due to the extreme significance of the Shuibuya CFRD, a large number of laboratory experiments [11,42] have been conducted on rockfill materials, including a series of triaxial experiments and creep experiments. These experimental data provide sufficient data to calibrate the constitutive parameters. In addition, abundant field displacement data have been collected during the construction, impounding and long-term operation, which can be used to check and correct the calibrated parameters. Tables 4 and 5 list the parameters determined based on the experimental and field observations given in the literature [11,42–44]. The zones of rockfill materials are indicated in Figure 9.

For concrete slabs and the toe plinth, the isotropic elasticity model is used, i.e., $E = 30$ GPa and $v = 0.167$. The contact behavior between the concrete slabs and the cushion material is modeled by the zero-thickness interface model
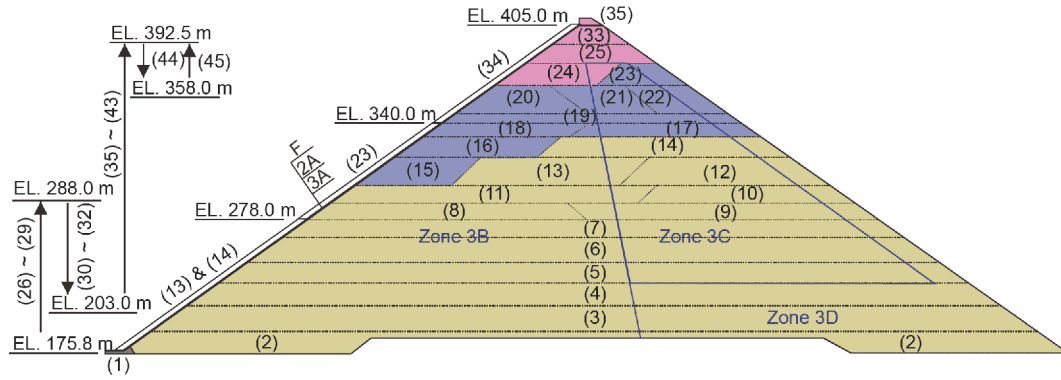
Figure 9   (Color online) Construction and impounding processes of the Shuibuya CFRD.

Table 4   Basic model parameters of rockfills used in Shuibuya CFRD

Material	φ_0 (°)	$\Delta\varphi$ (°)	d_0	ψ_0 (°)	$\Delta\psi$ (°)	k	n	α	k_{au}	v_e
2A & 3A	56.0	10.5	1.85	51.5	6.8	1000	0.38	1.22	2000	0.3
3B &3D	54.7	10.4	1.92	49.4	6.4	992	0.33	1.50	1824	0.3
3C	51.3	10.4	2.03	46.2	6.3	701	0.25	1.35	1402	0.3

Table 5   Creep model parameters of rockfills used in Shuibuya CFRD

Material	c_1 (%)	m_1	c_2 (%)	m_2	c_3 (%)	m_3	ω (month)
2A & 3A	0.16	0.45	0.006	0.88	0.032	0.66	5.5
3B &3D	0.16	0.45	0.006	0.88	0.032	0.66	5.5
3C	0.18	0.43	0.007	0.90	0.035	0.55	5.5

[45], and the parameters used are the same as those used in studying the deformation behavior of the Zipingpu CFRD using a generalized plasticity model [46]. The joint behavior between different slabs and the toe plinth are modeled using the parameters summarized by Gu et al. [47].

The stress induced deformation and creep of rockfill materials are generally considered separately in the current practice, i.e., creep during construction is neglected, and it starts after the completion of the dam filling or impounding. Field observations, however, show that creep deformation does occur during construction [17]. Back analysis using the field observations also shows that the obtained moduli of rockfill materials were considerably lower than the experimental values, and it was thought to be caused by the scale effect in experiments, the material inhomogeneity in the field and several other stochastic factors [42]. In the authors' opinion, neglecting the creep of rockfill materials during construction is another important cause of an underestimation of the deformation when using the experimental parameters. In this study, stress-induced deformation and creep of rockfill materials are considered simultaneously by using the proposed constitutive model. The creep behavior of each rockfill element is activated immediately after the filling of this element.

5.2   Results and interpretation

5.2.1   Deformation of the dam

Figure 10 compares the predicted settlement at the monitored points and the corresponding field observations made on 16 October, 2008. The predicted settlement at the lower three elevations, i.e., EL. 235.0 m, EL. 265.0 m and EL. 300.0 m, coincide well with the measured data both in the primary rockfill zone (3B) and in the secondary rockfill zone (3C). The numerical predictions at the upper two elevations, i.e., EL. 340. 0 m and EL. 370.0 m, however, display some deviation from the field observations. The settlements at EL. 340.0 m are underestimated while those at EL. 370.0 m are overestimated. Nevertheless, the general trends of the measured data are effectively reproduced by the finite element simulations, and it is reasonable to argue that the constitutive model as well as the used parameters are acceptable in modeling the behavior of rockfill materials used in the Shuibuya CFRD.

Figure 11(a) shows the contour of the horizontal displacement (along the *y* direction) and settlement at the section 0+212.0 m. Due to the hydrostatic pressure exerted upon the concrete slabs, a large portion of the dam displaces downstream. The horizontal displacement towards upstream
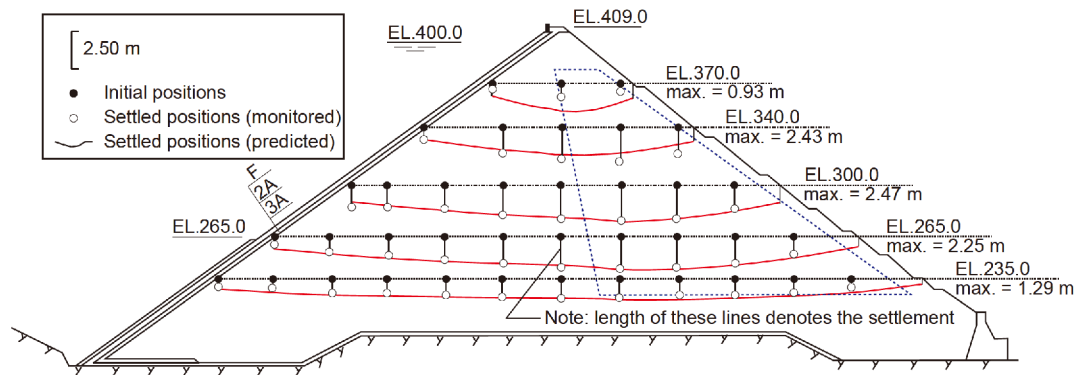
Figure 10   (Color online) Predicted settlement vs. measured settlement of the 0+212.0 mm section.
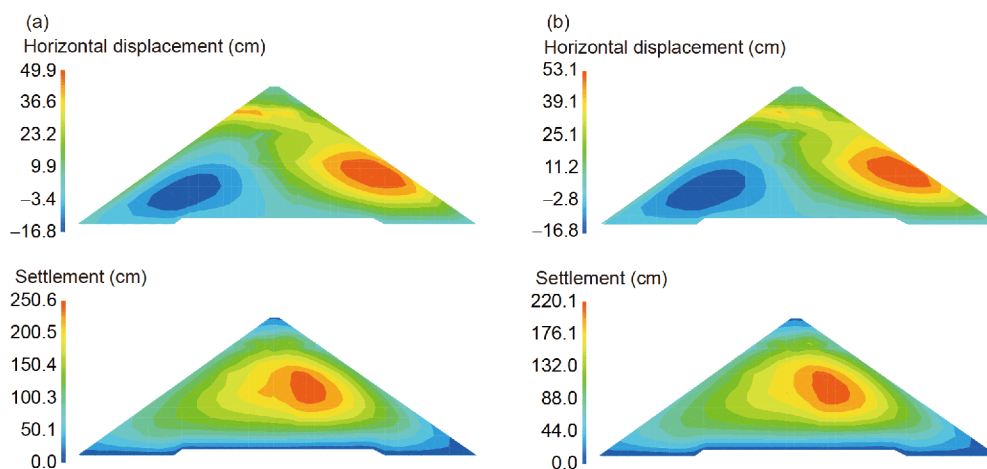
Figure 11   (Color online) Contours of the horizontal and vertical displacements in 0+212.0 section: (a) with creep; (b) without creep.

(max. = 16.8 cm) is evidently less than that towards downstream (max. = 49.9 cm). The settlement contour follows a ring-shaped distribution, with the peak region located in the secondary rockfill zone at the elevation of approximately half the dam height. As also shown in Figure 11(a), the rockfills within the 3C zone settle more than those within the 3B zone as a result of the higher compressibility of the former (Table 4). Field observations made on 16 October, 2008, show that a point within the 3C zone at EL. 300 m (Figure 10) settled a maximum of 247.2 cm, approximately 1.07% of the dam height. The maximal settlement predicted herein is 250.6 cm, which is quite close to the measured data.

The displacements predicted without consideration of the creep of rockfill materials are plotted in Figure 11(b) for comparison. Although the distributions of contours are almost the same as those plotted in Figure 11(a), the maximum displacements present some differences. In particular, the maximum settlement without creeping is 220.1 cm, considerably less than the observed value and that predicted by considering the creep of rockfill materials. The horizontal displacement is, however, smaller when considering the creeping effect, indicating that the shell of the dam contracts more when the creep is considered.

5.2.2   Deformation and stresses of the concrete slabs

Contours of the horizontal and perpendicular displacements of concrete slabs are shown in Figure 12(a). The concrete slabs at both the left bank and the right bank move towards the center of the canyon, with a maximum magnitude of 4.1 and 7.6 cm, respectively. This trend results in a compression in the concrete slabs near the center of the canyon. The red and blue regions in Figure 12(a) also suggest that the early cast concrete slabs may displace along the toe plinth during the filling of the rockfill materials afterward. The frictional forces exerted by the cushion rockfill as a result of axial displacement and settlement are responsible for such a deformation mode. The perpendicular displacement (deflection) of the concrete slabs also follows a ring distribution, the peak region of which is located in the first-stage slabs near the center of the canyon. In the current case, the maximum deflection measured is about 57.8 cm [40] and the numerical simulation predicts a maximum deflection of 53.4 cm, which is slightly lower than the observed value.

The horizontal displacement and deflection of the concrete slabs predicted without the creeping effect are shown in Figure 12(b). The axial displacement of the slabs in this case is slightly lower than the previous one given in Figure 12(a),

which may be attributed to the boundary restriction along the horizontal direction. Nevertheless, the deflection of the concrete slabs is evidently lower than the results given in Figure 12(a) and the observed value. This is a natural consequence of neglecting the creep of rockfill materials, which leads to an underestimation of the settlement of rockfill materials by nearly 12%.

Figure 13(a) shows the contours of the normal stresses within concrete slabs. The normal stress along the dam axis herein is actually the horizontal normal stress as the dam axis is a straight line. The normal stress along the upstream slope does not coincide with any stress component. However, it can be evaluated using the stress tensor and the unit vector of the slope direction. The horizontal displacement of the slabs

towards the center of the canyon results in compressive stresses within slabs near the center (especially the first stage slabs) and tensile stresses near the left and right abutments. The maximum magnitudes of the compressive and tensile stresses are 10.77 and 2.20 MPa, respectively. The normal stress along the slope direction is compressive almost everywhere with the only exception of the concrete slabs near the crest, where a maximum tensile stress of 0.44 MPa is predicted. Compared with the axial normal stress, the magnitude of the normal stress along the slope direction is much higher, particularly in the early cast concrete slabs. In the current case, the maximum compressive stress reaches 27.48 MPa, exceeding twice the magnitude of the axial normal stress.
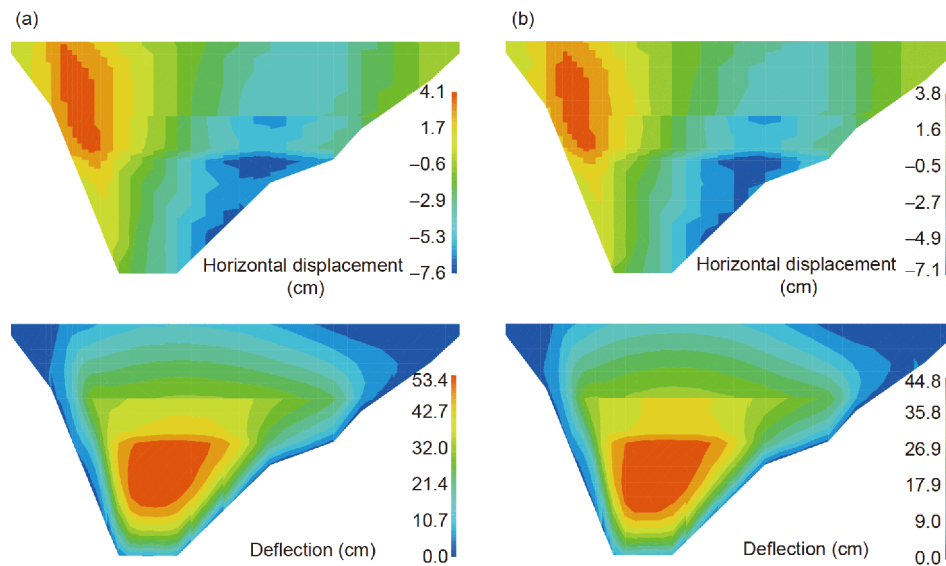

Figure 12 (Color online) Contours of the deformation of concrete slabs: (a) with creep; (b) without creep.
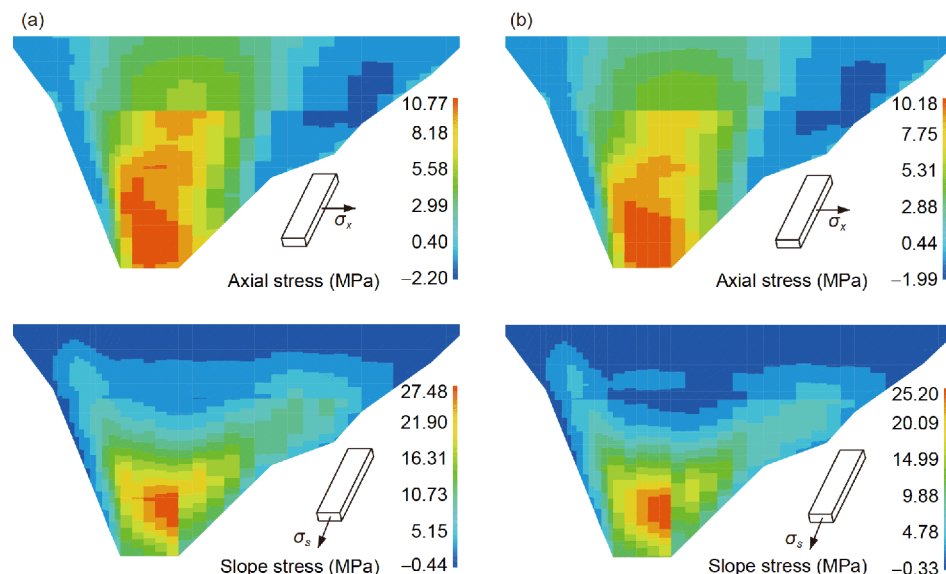

Figure 13 (Color online) Contours of the normal stresses within the concrete slabs: (a) with creep; (b) without creep.

Neglecting the creep of rockfill materials not only results in an underestimation of the deformation of the concrete slabs but also leads to an underestimation of stresses (particularly the slope stress) within the concrete slabs as shown in Figure 13(b). Less settlement of the underlying rockfill materials results in less frictional forces on the interfaces along the slope and thus a lower compressive stress within the early concrete slabs and a lower tensile stress within the slabs near the dam crest. The amount of deviation is approximately 8.3% in the current case.

6 Summary and conclusions

In this study, a constitutive model that can simulate the stress-induced strains and creep behavior of rockfill materials in a unified manner is established within the framework of generalized plasticity. The general forms of constitutive equations, both the stress-driven mode and the strain-driven mode, are derived using the concept of classical elastoplasticity. A key feature in the generalized plasticity formulations is the assumption of a single yield function for the judgment of the onset of plastic strains and two separate plastic potential functions for the directions of plastic strains caused by loading and creeping.

The plastic flow direction tensor, the loading direction tensor, the elastic tensor and the plastic modulus are defined to substantiate the basic model, and the creep flow direction tensor and the creep modulus are formulated to fulfill the modeling of the creep behavior. The model has a total of 10 parameters for the basic constitutive equation and 7 additional parameters for the modeling of the creep behavior. All these parameters can be calibrated using triaxial tests including triaxial compression, triaxial extension and triaxial creep experiments. The only exception is the parameter ω that controls the rate of creep strains. As the field conditions cannot be exactly reproduced in a laboratory, a rational way to determine this parameter is by using the available field observations or referring to similar engineering.

The proposed constitutive model is verified by triaxial compression experiments, true triaxial compression experiments and creep experiments on typical rockfill materials, and it is proved that the model is capable of capturing the salient features of rockfill materials, including the shear contraction and dilation, pressure dependent and path (Lode angle) dependent peak strength as well as the creep behavior. Thus, it is further used to study the deformation and stress behavior of the well-known Shuibuya concrete face rockfill dam. Since field observations indicated that creep deformation did occur during construction and impounding, numerical simulations are conducted with the creep model activated immediately after the filling of rockfill materials. Both the maximum settlement of the dam and the maximum

deflection of the concrete slabs agree well with the measured values in the field.

The numerical results also show that both the axial normal stress and the slope normal stress are compressive in most concrete slabs, except those near the left, right and top boundaries. In addition, for high CFRDs such as Shuibuya, concrete slabs are generally cast in several stages, and the early cast concrete slabs often bear high compressive stresses, particularly along the slope direction. This is caused by the downward frictional forces due to the settlement of underlying rockfill materials. It is also found that for high CFRDs with a long duration of construction, neglecting the creep of rockfill materials during construction may underestimate the deformation of the dam and the concrete slabs. In addition, the axial normal stress and the slope normal stress, both the compressive and tensile ones, will also be underestimated. Therefore, for extremely high CFRDs, the stress-induced strain and creep of rockfill materials are best considered simultaneously.

Finally, it deserves to point out that the model proposed in this study can reflect most of the important features of rockfill materials as mentioned previously, it cannot capture some other salient features observed in experiments, e.g., creep induced hardening behavior during post-creep loading and the altered creep behavior by previous unloading. Modeling these interaction effects between loading and creep needs more sophisticated models, which will be an important concern of the authors in the future.

Appendix: the function $g(\theta)$

The introduction of function $g(\theta)$ enables one to model the strength of rockfill materials under general stress states. To establish the representation of this function, the failure condition imposed by eq. (34) is rewritten as follows:

$$1 - \frac{q}{g(\theta)M_{\mathrm{f}}p} = 0, \tag{a1}$$

eq. (a1) can be interpreted in the following two different ways depending on the variable scaled by $g(\theta)$:

$$\frac{q/p}{[g(\theta)\cdot M_{\mathrm{f}}]} = 1; \quad \frac{[q/g(\theta)]}{M_{\mathrm{f}}\cdot p} = 1. \tag{a2}$$

The geometrical meanings of eq. (a2) are illustrated in Figure a1. The approach given by the first equation and that shown in Figure a1(a) can be seen as the traditional $g(\theta)$ method [19,20,48], the basic concept of which is to evaluate the peak stress ratio at the current Lode angle. Given a failure criterion, the peak stress ratio can be derived, with different levels of complexity in accordance with the used criterion. For instance, predicting the peak stress ratio using the criteria of Matsuoka et al. [34] and Lade [33] at a given Lode angle needs to solve a cubic algebraic equation.
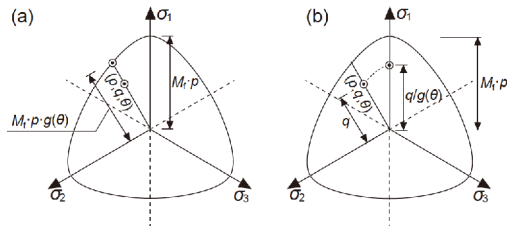
Figure a1   Geometrical interpretations of eq. (a2). (a) Traditional $g(\theta)$ method; (b) stress transformation approach.

The method given by the second equation in eq. (a2) and that plotted in Figure a1(b) can be seen as the stress transformation approach well developed by Yao et al. [34,35,49]. In this approach, the mobilized friction angle at any arbitrary stress state can be evaluated according to the used failure criterion, and the equivalent deviatoric stress under a triaxial compression stress state with the same mobilized friction angle can then be determined using eq. (32). In this study, the second approach is used due to its flexibility in incorporating three-dimensional failure criteria. To this end, the general form that satisfies eq. (a1) is rewritten as follows:

$$g(\theta) = \frac{q}{p} \cdot \frac{3 - \sin\varphi_m}{6\sin\varphi_m} = \frac{q}{2p}\left(\frac{1}{\sin\varphi_m} - \frac{1}{3}\right), \tag{a3}$$

in which the subscript m signifies the mobilized friction angle. The only thing left is to derive the representation of $\sin(\varphi_m)$ in terms of the stress variables. Table a1 gives the expressions of $\sin(\varphi_m)$ derived from the Mohr-Coulomb criterion, the Matsuoka-Nakai criterion [34] and the Lade criterion [33]. Herein, only the mobilized friction angle defined using Lade's criterion is demonstrated in detail. To this end, Lade's criterion [33] is rewritten as follows:

$$\frac{I_1^3}{I_3} = \frac{[(1+\sin\varphi_m)/(1-\sin\varphi_m)+2]^3}{(1+\sin\varphi_m)/(1-\sin\varphi_m)}. \tag{a4}$$

Introducing the following variable:

$$x_m = \frac{1+\sin\varphi_m}{1-\sin\varphi_m} + 2. \tag{a5}$$

Eq. (a4) can be simplified as follows:

$$x_m^3 - \frac{I_1^3}{I_3}x_m + 2\frac{I_1^3}{I_3} = 0, \tag{a6}$$

Table a1   Definition of mobilized friction angle in three failure criteria[a]

Criterion	Failure equation	Mobilized friction angle
Mohr-Coulomb	$\dfrac{\sigma_1 - \sigma_3}{\sigma_1 + \sigma_3} = \sin\varphi$	$\sin\varphi_m = \dfrac{\sigma_1 - \sigma_3}{\sigma_1 + \sigma_3}$
Matsuoka-Nakai	$\dfrac{I_1 I_2}{I_3} = \dfrac{9 - \sin^2\varphi}{1 - \sin^2\varphi}$	$\sin\varphi_m = \sqrt{\dfrac{I_1 I_2 - 9I_3}{I_1 I_2 - I_3}}$
Lade	$\dfrac{I_1^3}{I_3} = \dfrac{(3 - \sin\varphi)^3}{(1+\sin\varphi)(1-\sin\varphi)^2}$	$\sin\varphi_m = \dfrac{x_m - 3}{x_m - 1}$

a) $I_1 = \sigma_1 + \sigma_2 + \sigma_3$; $I_2 = \sigma_1 \cdot \sigma_2 + \sigma_2 \cdot \sigma_3 + \sigma_1 \cdot \sigma_3$; $I_3 = \sigma_1 \cdot \sigma_2 \cdot \sigma_3$.

eq. (a6) is a standard cubic algebraic equation, and the meaningful real solution of this equation can be derived ordinarily, i.e.,

$$x_m = 2\sqrt{\frac{I_1^3}{3I_3}}\cos\left\{\frac{1}{3}\arccos\left[-3\left(\frac{I_1^3}{3I_3}\right)^{-1/2}\right]\right\}. \tag{a7}$$

Substituting the obtained value of x_m into eq. (a7) gives the value of $\sin(\varphi_m)$, and it can be further substituted into eq. (a3) to obtain the corresponding $g(\theta)$ at any stress state. In this study, Lade's criterion is used for all the simulations.

1   Cooke J B. Progress in rockfill dams. J Geotech Engrg, 1984, 110: 1381–1414

2   International Commission on Large Dams (ICOLD). Concrete Face Rockfill Dams, Concepts for Design and Construction. Beijing: China Water Power Press, 2010

3   Xing H F, Gong X N, Zhou X G, et al. Construction of concrete-faced rockfill dams with weak rocks. J Geotech Geoenviron Eng, 2006, 132: 778–785

4   Won M S, Kim Y S. A case study on the post-construction deformation of concrete face rockfill dams. Can Geotech J, 2008, 45: 845–852

5   Zhang B, Wang J G, Shi R. Time-dependent deformation in high concrete-faced rockfill dam and separation between concrete face slab and cushion layer. Comput Geotechnics, 2004, 31: 559–573

6   Clements R P. Post-construction deformation of rockfill dams. J Geotechnical Eng, 1984, 110: 821–840

7   Dascal O. Postconstruction deformation of rockfill dams. J Geotech Eng, 1987, 113: 46–59

8   Hunter G, Fell R. Rockfill modulus and settlement of concrete face rockfill dams. J Geotechnical Geoenviron Eng, 2003, 129: 909–917

9   Feda J. Creep of Soils and Related Phenomena. Prague: Academia-Elsevier, 1992

10   Shen Z J, Zuo Y M. Study on rheology characteristics of rockfill. In: Proceedings of 6th Chinese Conference on Soil Mechanics and Foundation Engineering. Shanghai: Tongji University Press, 1991. 443–446

11   Cheng Z L, Ding H S. Creep test for rockfill. Chin J Geotech Eng, 2004, 26: 473–476

12   Oldecop L A, Alonso E E. Theoretical investigation of the time-dependent behaviour of rockfill. Géotechnique, 2007, 57: 289–301

13   Bauer E, Fu Z Z, Liu S H. Influence of pressure and density on the rheological properties of rockfills. Frontiers of Structural Civil Eng China, 2012, 6: 25–34

14   Fu Z Z, Chen S S, Liu S H. Hypoplastic constitutive modelling of the wetting induced creep of rockfill materials. Sci China Technol Sci, 2012, 55: 2066–2082

15   Dolezalova M, Hladik I. Constitutive models for simulation of field performance of dams. Int J Geomech, 2011, 11: 477–489

16   Wang H J, Yin Z Z. Creep tests of rockfill and double-yield surface creep model. Chin J Geotech Eng, 2008, 30: 959–963

17   Fu Z Z, Wang T B, Chen S S. Field observations made on four concrete face rockfill dams. In: Proceedings of the 4th International Conference on Civil Engineering and Urban Planning. Beijing, 2015. 589–595

18   Pastor M, Zienkiewicz O C, Chan A H C. Generalized plasticity and the modelling of soil behaviour. Int J Numer Anal Methods Geomech, 1990, 14: 151–190

19   Ling H I, Liu H. Pressure-level dependency and densification behavior

of sand through generalized plasticity model. J Eng Mech, 2003, 129: 851–860

20　Ling H I, Yang S. Unified sand model based on the critical state and generalized plasticity. J Eng Mech, 2006, 132: 1380–1391

21　Fu Z, Chen S, Peng C. Modeling cyclic behavior of rockfill materials in a framework of generalized plasticity. Int J Geomech, 2014, 14: 191–204

22　Zhang B, Chen T, Peng C, et al. Experimental study on loading-creep coupling effect in rockfill material. Int J Geomech, 2017, 17: 04017059

23　Fu Z, Chen S, Shi B. Large-scale triaxial experiments on the creep behavior of a saturated rockfill material. J Geotech Geoenviron Eng, 2018, 144: 04018039

24　Lade P V, Liggio Jr. C D, Nam J. Strain rate, creep, and stress drop-creep experiments on crushed coral sand. J Geotech Geoenviron Eng, 2009, 135: 941–953

25　Xiao Y, Liu H, Desai C S, et al. Effect of intermediate principal-stress ratio on particle breakage of rockfill material. J Geotech Geoenviron Eng, 2016, 142: 06015017

26　Xiao Y, Liu H, Liu H, et al. Strength and dilatancy behaviors of dense modeled rockfill material in general stress space. Int J Geomech, 2016, 16: 04016015

27　Nakai T. A unified mechanical quantity for granular materials in three-dimensional stresses. In: Proceedings of U.S./Japan Seminar on the Micromechanics of Granular Materials. Sendai-Zao, 1987. 297–307

28　Pradhan T B S, Tatsuoka F, Sato Y. Experimental stress-dilatancy relations of sand subjected to cyclic loading. Soils Found, 1989, 29: 45–64

29　Guo P J, Stolle D F E. The extension of Rowe's stress-dilatancy model to general stress condition. Soils Foundations, 2004, 44: 1–10

30　Kim M K, Lade P V. Single hardening constitutive model for frictional materials. Comput Geotechnics, 1988, 5: 307–324

31　Ottosen N S, Ristinmaa M. The Mechanics of Constitutive Modeling. London: Elsevier, 2005

32　Duncan J M, Chang C Y. Nonlinear analysis of stress and strain in soils. J Soil Mech Found Eng Division, ASCE, 1970, 96: 1629–1653

33　Lade P V. Assessment of test data for selection of 3-D failure criterion for sand. Int J Numer Anal Meth Geomech, 2006, 30: 307–333

34　Matsuoka H, Yao Y, Sun D. The cam-clay models revised by the smp criterion. Soils Found, 1999, 39: 81–95

35　Yao Y. Generalized non-linear strength theory and transformed stress

space. Sci China Ser E, 2004, 47: 691

36　Li G Y, Mi Z K, Fu H, et al. Experimental studies on rheological behaviors for rockfills in concrete faced rockfill dams. Rock and Soil Mechanics, 2004, 25: 1712–1716

37　Ling H, Han H Q, Shi B X. Experimental Research on the Engineering Properties of the Fill Materials Used in the Dashixia Concrete Faced Rockfill Dam. Research Report. Nanjing: Nanjing Hydraulic Research Institute, 2017

38　Shi W C. True Triaxial Tests on Coarse-Grained Soils and Study on Constitutive Model. Dissertation for Dcotoral Degree. Nanjing: Hehai University, 2008

39　Fu H, Ling H. Experimental Research on the Engineering Properties of the Fill Materials Used in the Cihaxia Concrete Faced Rockfill Dam. Research Report. Nanjing: Nanjing Hydraulic Research Institute, 2009

40　Rodriguez N M, Lade P V. True triaxial tests on cross-anisotropic deposits of fine Nevada sand. Int J Geomech, 2013, 13: 779–793

41　Fu Z Z, Chen S S. Stress and Consolidation Analysis Program for Earth and Rockfill Structures (SCAPERS), Theory and Manual. Research Report. Nanjing: Nanjing Hydraulic Research Institute, 2014

42　Yang Q G, Liu N, Sun Y, et al. Construction Technologies in the Shuibuya Concrete Face Rockfill Dam. Beijing: China Water Power Press, 2010

43　Zhou W, Hua J, Chang X, et al. Settlement analysis of the Shuibuya concrete-face rockfill dam. Comput Geotechnics, 2011, 38: 269–280

44　Zhou X, Ma G, Zhang Y. Grain size and time effect on the deformation of rockfill dams: A case study on the Shuibuya CFRD. Géotechnique, 2018, 1–14

45　Goodman R E, Taylor R L, Brekke T L. A model for the mechanics of jointed rock. J Soil Mech Found Division, ASCE, 1968, 94: 637–659

46　Xu B, Zou D, Liu H. Three-dimensional simulation of the construction process of the Zipingpu concrete face rockfill dam based on a generalized plasticity model. Comput Geotechnics, 2012, 43: 143–154

47　Gu G C, Shu Y M, Shen C S. Experiences and Innovations in Earth and Rockfill Dam Engineering. Beijing: China Electric Power Press, 2004

48　Zienkiewicz O C, Pande G N. Some useful forms of isotropic yield surfaces for soil and rock mechanics. Gudehus G, ed. In: Finite Elements in Geomechanics. Chichester: Wiley. 1977. 179–190

49　Yao Y P, Wang N D. Transformed stress method for generalizing soil constitutive models. J Eng Mech, 2014, 140: 614–629